ACS APPLIED MATERIALS & INTERFACES

www.acsami.org

Research Article

Atomistic Modeling of the Effect of Temperature on Interfacial Properties of 3D-Printed Continuous Carbon Fiber-Reinforced Polyamide 6 Composite: From Processing to Loading

Shenru Wang, Xin Yan,* Baoning Chang, Siqin Liu, Lihua Shao, Wuxiang Zhang,* Yingdan Zhu,* and Xilun Ding

Cite This: https://doi.org/10.1021/acsami.3c12372

Read Online

ACCESS | Metrics & More | Article Recommendations

ABSTRACT: The combination of continuous fiber-reinforced thermoplastic composites (CFRTPCs) and the continuous fiber 3D printing (CF3DP) technique enables the rapid production of complex structural composites. In these 3D-printed composites, stress transfer primarily relies on the fiber−resin interface, making it a critical performance factor. The interfacial properties are significantly influenced by the temperatures applied during the loading and forming processes. While the effect of the loading temperature has been extensively researched, that of the forming temperature remains largely unexplored, especially from an atomistic perspective. Our research aims to employ molecular dynamics simulations to elucidate the effect of temperature on the interfacial properties of continuous carbon fiber-reinforced polyamide 6 (C/PA6) composites fabricated using the CF3DP technique, considering both loading and forming aspects. Through molecular dynamics simulations, we uncovered a positive correlation between the interfacial strength and forming temperature. Moreover, an increased forming temperature induced a notable shift in the failure mode of C/PA6 under uniaxial tensile loading. Furthermore, it was observed that increasing loading temperatures led to the deterioration of the mechanical properties of PA6, resulting in a gradual transition of the primary failure mode from adhesive failure to cohesive failure. This shift in the failure mode is closely associated with the glass transition of PA6.

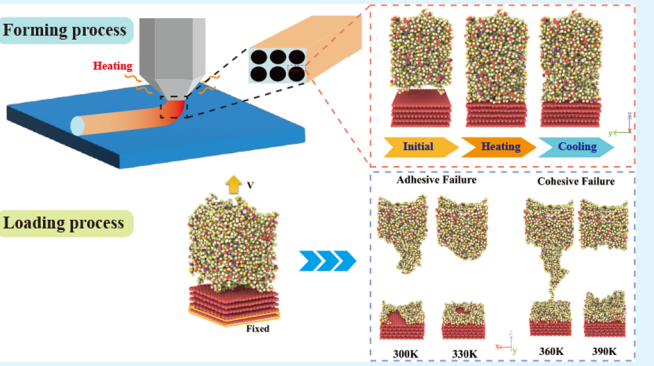

KEYWORDS: *3D printing, continuous fiber-reinforced thermoplastic composite, interface, molecular dynamics simulation, forming mechanism*

1. INTRODUCTION

Continuous fiber-reinforced thermoplastic composites (CFRTPCs) are extensively utilized in various applications because of their remarkable features, such as being lightweight and their high mechanical strength, excellent thermal stability, chemical resistance, and recyclability.[1−5] These applications span across diverse sectors, including aerospace,[6,7] automobile,[8,9] and marine[10] industries. Continuous fiber three-dimensional (3D) printing (CF3DP) is a brand new manufacturing approach for CFRTPCs. This approach is based on a layer-by-layer principle, which enables the rapid production of complex structural composites.[11−13] The in situ impregnation technique shown in Figure 1a is a promising CF3DP strategy. It impregnates the continuous dry fiber with the thermoplastic within the printing head during the forming process. This technique offers distinct advantages, including the accurate control of the fiber volume fraction and the diverse selection of material types. Raw materials are conveyed to the molten cavity (Figure 1a) and heated to a molten state at a specific temperature. The printing head follows a predetermined path and deposits the material onto the printing bed. Once the material is extruded, it cools and solidifies to form the structure.

The interfacial strength of the 3D-printed composites plays a pivotal role in determining the performance of CFRTPCs.[14] Previous studies have demonstrated that a weaker interface tends to result in the premature failure of the composite parts, occurring before they reach their intended load-bearing limit.[15−17] Temperature plays a vital role in determining the

Received: August 19, 2023
Revised: October 27, 2023
Accepted: October 30, 2023

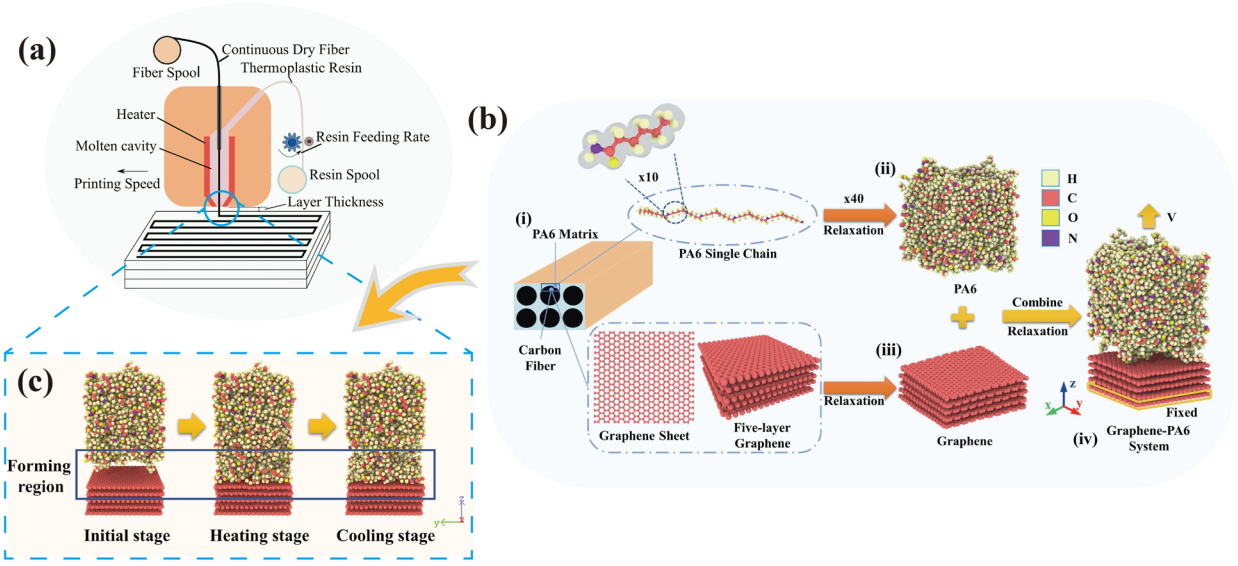

Figure 1. (a) Schematic diagram of the continuous fiber 3D printing process (in situ impregnation approach). (b) Conformations of all-atom model of the C/PA6 system. (c) Snapshots of the interface formation process of the C/PA6 system, which was heated at 500 K and then cooled to 300 K.

interfacial properties, and it contains two aspects.[15,18] First, during the loading process, the interfacial properties are affected by the loading temperature. This temperature refers to the ambient temperature at which a composite product is utilized. Second, during the formation process, the interfacial properties are susceptible to the influence of the forming temperature. This temperature refers to the specific processing temperature that is necessary for composite production during the CF3DP process.

The effect of temperature on the interfacial properties of printed CFRTPCs has been investigated in the past, particularly the loading temperature. Previous experimental and theoretical research has revealed that exposure to elevated temperatures leads to a degradation of the mechanical properties of thermoplastics, which consequently affects the interfacial properties.[18−22] However, there is a lack of extensive research examining the influence of the forming temperature on interfacial properties. Previous studies have primarily relied on macro-experiments and have observed a significant improvement in mechanical properties with increasing forming temperature.[15,23,24] Nevertheless, these studies lack a comprehensive understanding of the microscopic mechanisms underlying the influence of the temperature on the interfacial properties. Typically, the interaction between the polymer and the fiber at the molecular level determines the interfacial properties, which, in turn, significantly impact the macro performance of CFRTPCs.[3,25] Therefore, a nanoscale perspective that delves into the adhesive mechanism, mechanical properties, and failure mechanism of the interface is imperative.

Molecular dynamics (MD) simulation is an effective method for examining the atomic-scale interfacial properties of composites.[26] Even though a great effort has been taken to study the interfacial properties of CFRTPCs and great progress has been made, there remains a notable gap in utilizing MD simulations to systematically analyze the effect of temperature on the composite interface fabricated through CF3DP.[3,25−31] The CF3DP process possesses a distinctive characteristic: the combination of fibers and resins as well as the formation of composite products occurs simultaneously. The interface formation that occurs during this process plays a vital role in determining the performance of the composite. Unfortunately, this interface formation process cannot be observed visually from an atomistic point of view. Thus, to overcome this limitation and gain a comprehensive understanding of the effect of temperature on the interface formation process, MD analysis becomes necessary. Additionally, continuous carbon fiber-reinforced polyamide 6 (C/PA6) composites have garnered significant attention among the materials commonly utilized in the CF3DP process.[32] Consequently, we chose C/PA6 as the subject of our study.

In this study, we investigated the effect of temperature on the interfacial properties of a C/PA6 composite fabricated via CF3DP from an atomistic point of view. The results obtained from this study will serve as a valuable reference for determining the optimal forming temperature of CF3DP and provide insights into the bonding and fracture mechanisms of printed C/PA6 composites.

2. SIMULATION MODEL AND METHODOLOGY

2.1. Model Description. For the 3D-printed CFRTPCs depicted in Figure 1b(i), the size of the fiber−resin interface is at the nanoscale level. To investigate the interfacial bonding mechanism of the C/PA6 composite during the CF3DP process, an atomistic model of the C/PA6 interface was constructed. Prior to assembling the C/PA6 system, separate atomistic models of PA6 and carbon fiber were developed. To facilitate a more straightforward exploration of the interface formation mechanism, we took the simplest case in which the carbon fiber had not undergone surface modification.[33−35] Moreover, because graphene has no charge, we primarily considered the contribution of van der Waals (vdW) forces in the composite interface in our research.[33,34,36]

The amorphous PA6 was constructed with a target density of 1.15 g/cm^3.[37] The PA6 model consisted of 40 polymer chains with 10 repeat units in each chain. Figure 1b(ii) displays the PA6 model with side lengths of 42.60 Å × 39.35 Å × 56.47 Å.

The surface of continuous carbon fiber is primarily composed of aromatic rings.[3] Therefore, a multilayer graphene model was employed to represent the surface of continuous carbon fiber in the molecular simulation.[3] Figure 1b(iii) illustrates the multilayer

https://doi.org/10.1021/acsami.3c12372
ACS Appl. Mater. Interfaces XXXX, XXX, XXX−XXX

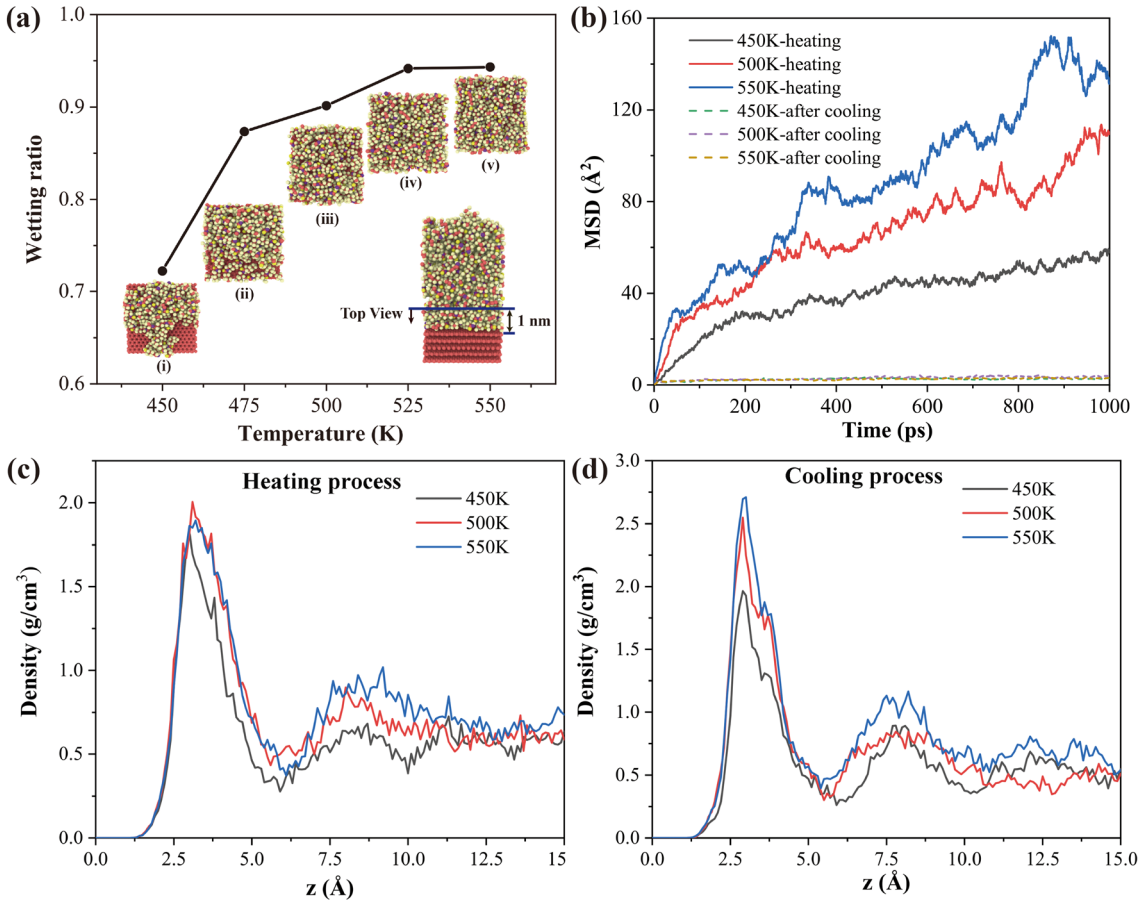

Figure 2. (a) Wetting ratio of C/PA6 interfaces at different forming temperatures. (b) MSD−time curves of the PA6 backbone under different forming temperatures. Local density distribution of PA6 along the *z*-direction at the interface during both the (c) heating and (d) cooling processes.

graphene model, in which the bond length of C−C was 1.42 Å,[38] the size of a single graphene sheet was 42.60 Å × 39.35 Å, and the stacking distance was 3.40 Å.[38,39]

The all-atom composite model shown in Figure 1b(iv) was composed of the graphene and PA6 model. There were 7680 atoms in the PA6 model and 3200 atoms in the graphene model. Both the initial graphene and PA6 models were equilibrated at 300 K with the microcanonical (NVE) ensemble for 100 ps, followed by the canonical (NVT) ensemble for 1 ns. The time step that was adopted in the simulation was 1 fs.

2.2. Simulation Procedures. In this study, MD simulations were performed using Large-scale Atomic/Molecular Massively Parallel Simulator (LAMMPS),[40] and atomic imaging was performed in OVITO.[41] The adaptive intermolecular reactive empirical bond order potential (AIREBO) was used to describe the atomistic interactions of graphene.[42] The polymer consistent force field (PCFF) was utilized to represent both the inter- and intramolecular interactions within PA6, as well as the interactions between graphene and PA6.[43,44] PCFF is valid for accurately capturing various conformational changes in organic materials, including the interactions between graphene and various thermoplastics.[45] The cutoff radius was 10 Å. The long-range electrostatics were calculated by the particle−particle particle−mesh (PPPM) algorithm with an accuracy of 10^{-4}. Periodic boundary conditions (PBCs) were applied in the *x*- and *y*-directions, and a nonperiodic boundary condition was used in the *z*-direction.

The interface forming process comprises two main stages: the heating process and the cooling process. The heating process simulation was conducted at different temperatures (450, 475, 500, 525, and 550 K) using the NVT ensemble with a total simulation time of 1 ns. After that, the C/PA6 system was gradually cooled to 300 K to simulate the cooling process. Because of the short formation time of the interface during the printing process, the formed interface of the printed parts is not perfect. Moreover, we remarked that, due to the size and time scale limitations of MD, the atomistic simulation might not capture the complete picture of the 3D printing process. However, we would like to shed a qualitative light on understanding how the variation of temperature during 3D printing impacts the interfacial property from an atomistic point of view. Therefore, we constructed a C/PA6 molecular model and simulated the interface formation process from an atomistic point of view. In the construction of the C/PA6 model, PA6 was positioned above graphene, and the distance between them was 7.5 Å, which was less than the cutoff radius of the nonbonded forces. The bottom layer of graphene and the top atoms of PA6 were then fixed while allowing enough free atoms to facilitate the formation of an interface. This treatment can approximately simulate the constraint situations of the fiber and resin components in the actual printing process. Essentially, it prevents the entire resin component from migrating to the fiber surface solely through nonbonded forces while ensuring an adequate number of free atoms to accurately simulate the interface formation.

In addition, to analyze the mechanical properties of the C/PA6 interface that formed at different forming temperatures, tensile loading was applied by moving the top atoms of PA6 at a constant velocity of 10^{-5} Å/fs along the *z*-axis while keeping the bottom layer of graphene fixed, as shown in Figure 1b(iv). This tensile simulation was performed under the NVT ensemble at 300 K. To further explore the effect of loading temperature on the mechanical properties and fracture mechanism of the C/PA6 interface, additional uniaxial tensile simulations were performed under the NVT ensemble at different loading temperatures (300, 330, 360, and 400 K).

https://doi.org/10.1021/acsami.3c12372
ACS Appl. Mater. Interfaces XXXX, XXX, XXX−XXX

3. RESULTS AND DISCUSSION

3.1. Interface Formation Process. The interface formation process is depicted in Figure 1c. At the initial stage, there was a visible gap between PA6 and graphene, which was called the forming region. As the simulation proceeded, the atoms within the C/PA6 system exhibited violent movement due to the high temperature, marking the heating stage. At this stage, the attractive vdW forces pulled the atoms of PA6 and graphene toward each other, resulting in the formation of an interface. During the heating stage, it was observed that the PA6 atoms were evenly distributed in the forming region. Upon entering the cooling stage, the mobility of the atoms decreased. As a consequence, the atoms within the forming region exhibited heightened susceptibility to the attractive forces exerted by the neighboring PA6 cluster and graphene. Specifically, the upper atoms in the forming region gradually moved toward the PA6 cluster, whereas the lower atoms moved closer to the graphene, thereby resulting in the stacking of more atoms in the interface.

3.2. Effect of Forming Temperature on Interfacial Bonding Properties. *3.2.1. Wettability.* Wettability is a critical property that characterizes the capacity of the resin matrix to wet the fiber surface. By enhancing wettability, a significantly larger resin matrix area can adhere to the fiber surface, thereby resulting in notable improvements in the interfacial properties.[46] To assess the wettability of the system, we employed the wetting ratio, which involved calculating the proportion of the graphene surface area covered by PA6 atoms to the total surface area of graphene. This calculation was performed using the following equation:

$$\text{Wetting ratio} = \frac{S_{PA}}{S_G} \tag{1}$$

where S_{PA} represents the graphene surface area covered by PA6 atoms and S_G represents the total surface area of graphene.

To investigate the effect of the forming temperature on wettability, we conducted an analysis of the wetting ratio for the C/PA6 interfaces. These interfaces were formed by heating the system at different temperatures and then cooling it to room temperature (300 K). The calculation results are visually represented in Figure 2a, along with the top views of the sliced samples (the samples were sliced at 1 nm away from the graphene surface) for each interface formed at different temperatures: (i) 450, (ii) 475, (iii) 500, (iv) 525, and (v) 550 K. As the interface forming temperature increased from 450 to 550 K, the wetting ratio increased from 0.72 to 0.94. This indicates that at higher forming temperatures, an increased number of PA6 atoms stack onto the graphene surface, leading to enhanced nonbonded interactions between the two components. However, as the forming temperature continues to rise, the rate of the wetting ratio increase begins to slow. This behavior can be attributed to there being a saturation of stacked atoms at the interface.

3.2.2. Mean Square Displacement. The interface formation process is closely related to the motility of PA6 atoms with a forming temperature change. The influence of temperature on the mobility of PA6 can be elucidated by examining the mean square displacement (MSD) of the backbone carbon atoms of PA6.[47,48] MSD can be calculated by eq 2:[49]

$$\text{MSD}=\frac{1}{N}\sum_{i=1}^{N} |\vec{R}_i(t) - \vec{R}_i(0)|^2 \tag{2}$$

where $\vec{R}_i(t)$ denotes the position of atom i at time t, $\vec{R}_i(0)$ denotes the position of atom i at the initial stage, and N is the total number of PA6 atoms.

Figure 2b depicts the MSD−time curves of the backbone carbon atoms of PA6. The solid lines represent the MSD values at various forming temperatures during the heating process, while the dashed lines represent the MSD values after cooling from these varied forming temperatures to 300 K. During the heating process, the rate of the MSD increase rises with the forming temperature, indicating that high temperatures promote the mobility of PA6. Consequently, at higher temperatures, PA6 can diffuse more easily onto the graphene surface, establishing nonbonded interactions with its atoms. However, as the temperature cools to 300 K, it can be observed in Figure 2b that there is a noticeable decrease in the rate of the MSD increase compared to that during the heating process. This observation suggests that a low temperature freezes the PA6 chains and limits their mobility.

3.2.3. Local Density Distribution. In essence, the strength of the interfacial nonbonded interactions increases with the local density of PA6 at the interface. Consequently, gaining insights into the local density distribution of PA6 during the formation of the interface is crucial for understanding the effect of the forming temperature on the interfacial bonding properties. To achieve this, we conducted comprehensive calculations of the local density distribution of PA6 along the z-direction at the interface during both the heating and cooling processes.

The results, depicted in Figure 2c,d, utilize the upper surface of graphene as the reference point with z = 0 Å. Figure 2c,d visually reveals that the density reaches its maximum value at approximately 2.75 Å, indicating the location of the C/PA6 interface. Specifically, Figure 2c displays the density distribution of PA6 during the heating process, highlighting that the density peak exhibits an initial increase followed by a subsequent decrease with increasing forming temperature, reaching a turning point at 500 K. Likewise, Figure 2d depicts the density distribution of PA6 during the cooling process, indicating a continuous increase in the density peak with forming temperature. It is worth noting that the density peak that was achieved during the cooling process significantly surpasses that of the heating process. The correlation between the local density and forming temperature partly reflects the trend in interfacial strength, a phenomenon that will be quantitatively analyzed in the subsequent section.

3.2.4. Interfacial Bonding Energy. The effect of the forming temperature on the C/PA6 interface was quantitatively examined by assessing the interfacial bonding energy. The interfacial bonding energy represents the interaction energy between PA6 and graphene and is widely used to gauge the interfacial bonding strength.[25,50] A higher interfacial bonding energy indicates a more stable interface structure and a stronger interfacial bonding strength. Because the energy of each component includes their interaction energy, the interfacial bonding energy can be obtained by subtracting the total energy of the C/PA6 system from the sum of the energy of both components:

$$E_{\text{interface}} = E_{\text{PA6}} + E_{\text{graphene}} - E_{\text{total}} \tag{3}$$

Here, $E_{\text{interface}}$, E_{PA6}, E_{graphene}, and E_{total} represent the interfacial bonding energy, energy of PA6, energy of graphene, and total energy of the simulation system, respectively.

https://doi.org/10.1021/acsami.3c12372
ACS Appl. Mater. Interfaces XXXX, XXX, XXX−XXX

The relationship between the interfacial bonding energy and the forming temperature is depicted in Figure 3, enabling an analysis of the effect of temperature on the interface formation during both the heating and cooling processes. In the heating process, the interfacial bonding energy exhibits an increase from 276.03 to 348.81 kcal/mol as the forming temperature rises from 450 to 500 K. However, when the forming temperature reaches 550 K, the interfacial bonding energy decreases to 334.80 kcal/mol. In the cooling process, it is evident that the interfacial bonding energy exhibits an increase at various forming temperatures compared to the heating process. Moreover, as the forming temperature rises from 450 to 550 K, the interfacial bonding energy shows a consistent rise from 294.08 to 403.18 kcal/mol for the cooling process. Clearly, the observed trend in the interfacial bonding energy closely aligns with the trend observed in the local density.

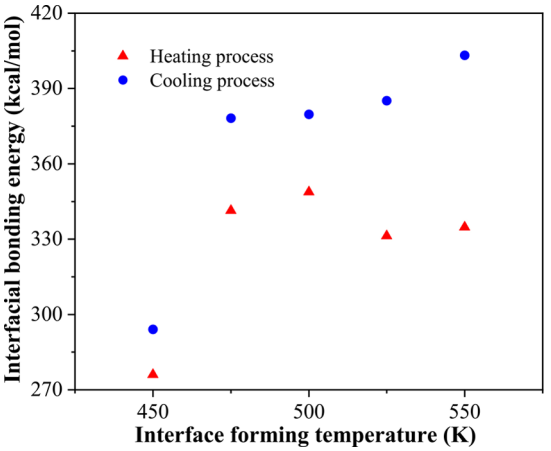

Figure 3. Interfacial bonding energy with different forming temperatures during both the heating and cooling processes.

Building upon the analysis presented in the preceding sections, distinctive trends in the interfacial bonding energy can be elucidated. In the heating process, the trend of the interfacial bonding energy that exists when the temperature changes from 450 to 500 K suggests that elevating the forming temperature increases the nonbonded interactions between PA6 and graphene. This enhancement is attributed to the increased mobility of PA6, which allows for more PA6 atoms to disperse into the forming region and establish interfaces with the graphene atoms through nonbonded interactions. However, the interfacial bonding energy decreases to 334.80 kcal/mol when the forming temperature increases from 500 to 550 K. This decline can be explained with the conclusion in section 3.2.1, which stated that the degree of accumulation of PA6 atoms at the interface reaches saturation when the temperature surpasses 500 K. Simultaneously, when the forming temperature exceeds the melting point of PA6 (500 K),[51] the elevated temperature induces an expansion in the intermolecular distance, leading to a decrease in the nonbonded interactions at the interface.

In the cooling process, the interfacial bonding energy experiences a notable increase compared with the heating process. Additionally, the interfacial bonding energy monotonically increases with the forming temperature. According to the discussion in section 3.1, the atomic kinetic energy decreases as the C/PA6 system cools down, causing the PA6 atoms to

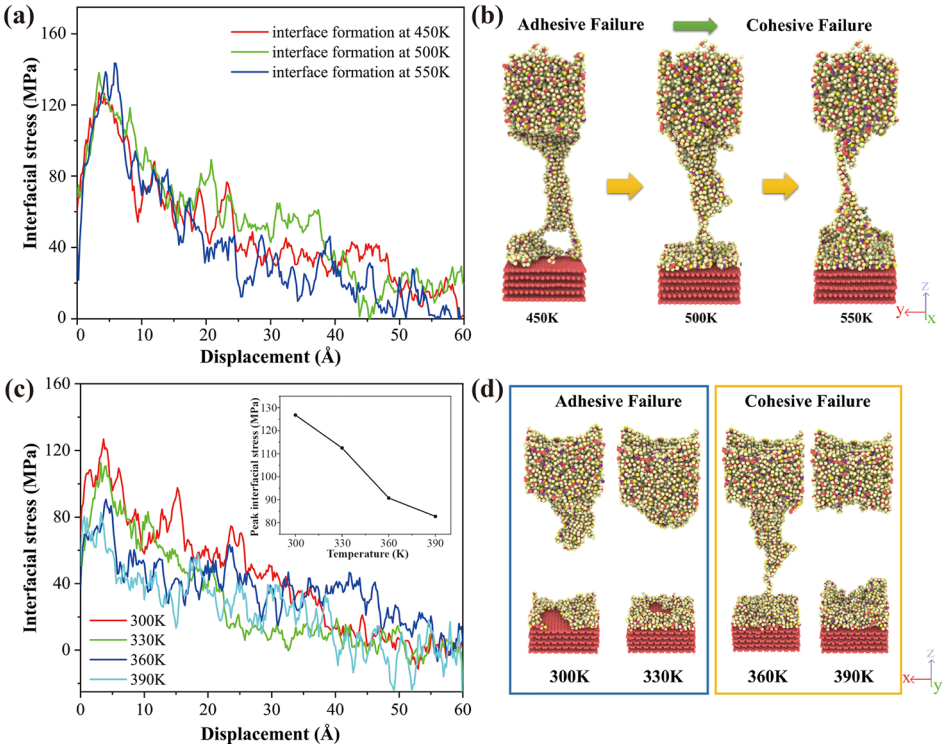

Figure 4. (a) Interfacial stress−displacement curves of C/PA6 composites (formed at either 450, 500, or 550 K) loaded at 300 K. (b) Snapshots of the fracture morphologies of C/PA6 composites (formed at either 450, 500, or 550 K) loaded at 300 K. (c) Interfacial stress−displacement curves of C/PA6 composites (formed at 500 K) loaded at various loading temperatures (300, 330, 360, and 390 K). (d) Snapshots of the fracture morphologies of C/PA6 composites (formed at 500 K) loaded at different loading temperatures (300, 330, 360, and 390 K).

https://doi.org/10.1021/acsami.3c12372
ACS Appl. Mater. Interfaces XXXX, XXX, XXX−XXX

gradually accumulate at the interface due to nonbonded interactions. Consequently, this results in an augmented interfacial bonding energy during the cooling process. Furthermore, due to the increased mobility of PA6 when the forming temperature exceeds 500 K, a higher concentration of active PA6 atoms is present in the forming region during the heating process. Thus, during the subsequent cooling process, these atoms exhibit a greater propensity to migrate toward the graphene, thereby intensifying the interfacial nonbonded interactions.

3.2.5. Uniaxial Tensile Deformation. The preceding section delved into the effect of the forming temperature on the interfacial bonding properties, considering it from an energetic standpoint. We are also interested in the influence of the forming temperature on the mechanical properties of the interface. Therefore, to analyze the influence of the forming temperature on the mechanical behavior of the C/PA6 interface, uniaxial tensile deformation simulations were conducted on the C/PA6 interface models created at different forming temperatures. The models that were employed in this separation simulation were initially prepared at the forming temperatures of 450, 500, and 550 K, respectively. Subsequently, the models were gradually cooled to room temperature (300 K). These separation simulations were carried out with the loading temperature of 300 K.

Figure 4a illustrates the correlation between the interfacial tensile stress and the tensile displacement of C/PA6. The curves were smoothed by using the adjacent averaging method. For all cases, the interfacial stress increased linearly in the initial stage and reached a peak value before entering a yield region, where the stress decreased gradually with increasing displacement. Figure 4a clearly illustrates that there is a positive correlation between the forming temperature and the interfacial stress peak. As the forming temperature increases from 450 to 550 K, there is a noticeable increase in the interfacial stress peak from 126.9 to 143.6 MPa. This phenomenon can be attributed to the fact that a higher forming temperature facilitates the formation of a C/PA6 interface with enhanced interfacial properties, as evidenced by the findings presented in section 3.2.4. Consequently, a greater amount of energy is required to disrupt this interface due to its increased strength.

The failure mechanism of the C/PA6 system under tensile loading is of crucial significance. To investigate the effect of the forming temperature on this mechanism, the fracture morphologies of C/PA6 were extracted from the calculated results at various forming temperatures. The C/PA6 models were stretched with a displacement of 50 Å, and the resulting fracture morphologies are displayed in Figure 4b. From the observations in Figure 4b, it becomes evident that at a forming temperature of 450 K, a substantial number of PA6 atoms progressively detach from the interface under the tensile load, leaving only a small fraction of atoms at the interface. However, as the forming temperature increases, a substantial number of PA6 atoms detach from the PA6 cluster and accumulate at the interface. This finding indicates that the C/PA6 interfaces formed at higher temperatures exhibit enhanced interfacial strength during the stretching process and are less prone to damage under tensile loading. These results are consistent with the conclusions presented in Figure 4a.

Furthermore, an analysis of the fracture morphologies reveals two distinct failure modes during the stretching process: adhesive failure and cohesive failure. Adhesive failure occurs when polymer chains detach from the interface, while cohesive failure arises when polymer chains pull away from the molecular cluster of PA6. Typically, both failure modes coexist with one mode prevailing, depending on the strength of the C/PA6 interface and PA6 itself. When the interfacial strength is lower than the strength of the polymer, damage at the interface is more likely to occur and adhesive failure dominates. Figure 4b illustrates this relationship. For instance, at a forming temperature of 450 K, the interfacial strength is relatively weak, leading to dominant adhesive failure. As the forming temperature increases, the interfacial strength improves and gradually surpasses the strength of the polymer, resulting in a transition from adhesive failure to cohesive failure. In summary, this analysis of the C/PA6 system under tensile loading at different forming temperatures reveals that the interfacial strength plays a critical role in determining the failure mechanism. Understanding these aspects can help optimize the forming process to achieve superior interfacial strength and reduce the likelihood of damage during tensile loading.

3.3. Effect of Loading Temperature on the Interfacial Mechanical Properties and Fracture Mechanism. In the study of C/PA6 composites, the interfacial properties are affected not only by the forming temperature but also by the loading temperature during mechanical loading. To investigate the mechanical properties and fracture mechanism of the C/PA6 interface at different loading temperatures (300, 330, 360, and 390 K), a series of uniaxial tensile simulations were conducted. The C/PA6 interface model was initially prepared at a forming temperature of 500 K. Figure 4c illustrates the interfacial stress−displacement curves for the separation between graphene and PA6 at different loading temperatures. The curves were smoothed using the adjacent averaging method. It is evident that all of the curves exhibit two distinct regions. The initial stage is characterized by a finite linear elastic region, which is subsequently followed by a yield region. Remarkably, the peaks of the curves predominantly occur at a tensile displacement of 5 Å. A noteworthy observation is that the interfacial tensile stress peak of C/PA6 gradually decreases with an increase in the loading temperature. Therefore, we can conclude that higher loading temperatures lead to a decrease in the mechanical properties of the C/PA6 interface.

As the loading temperature rises from 300 to 330 K, the interfacial stress peak decreases from 126.77 to 112.53 MPa, resulting in an approximate 11% decrease. Subsequently, as the temperature further increases to 360 K, the peak value undergoes a significant decrease to 90.71 MPa, representing a reduction of about 19% compared to the peak value at 330 K. Upon reaching 390 K, the peak value experiences a gradual decline to 82.75 MPa, which is approximately 9% lower than the peak value at 360 K. The interfacial stress peak−temperature diagram, located in the upper right corner of Figure 4c, clearly illustrates this variation trend. A detailed examination of the data reveals that the decline in the interfacial stress peak is less pronounced within the temperature ranges of 300−330 K and 360−390 K, while a sudden decrease in the interfacial stress peak occurs between 330 and 360 K. Consequently, it can be concluded that two distinct tensile failure mechanisms are at play at different loading temperatures, with the transition point of the failure mechanism falling within the interval of 330−360 K.

Figure 4d shows snapshots that capture the tensile failure of the C/PA6 model at an identical tensile displacement of 60 Å.

https://doi.org/10.1021/acsami.3c12372
ACS Appl. Mater. Interfaces XXXX, XXX, XXX−XXX

The figure reveals two distinct failure modes: adhesive failure and cohesive failure. At temperatures of 300 and 330 K, the failure snapshots indicate that a significant portion of the PA6 detaches from the interface during low-temperature stretching. This observation suggests that adhesive failure predominates during this condition, signifying that the strength of the interface is weaker compared to the strength of PA6. Conversely, at temperatures of 360 and 390 K, the failure snapshots demonstrate that, during high-temperature stretching, most of the PA6 chains pull away from the molecular clusters and progressively accumulate at the interface throughout the stretching process. This indicates that cohesive failure dominates during this scenario, implying that the strength of the interface is higher than that of PA6. The primary factor contributing to the shift in the failure mode is the degradation of the mechanical properties of PA6.

We elucidate the primary factor contributing to the transition of the failure mode at the molecular level by employing calculations of PA6 mobility. We computed the MSD for PA6 at various temperatures over a period of 1 ns. The resulting MSD curve can be approximated as a straight line, where the slope of this line reflects the mobility of PA6. Figure 5 illustrates the relationship between the MSD slope of

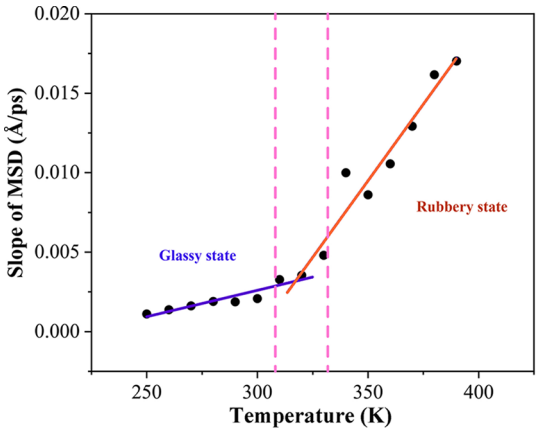

Figure 5. Slope of MSD of the PA6 backbone at different temperatures.

the PA6 backbone and temperature. As the temperature rises, the MSD slope increases, and the data points can be fitted using two distinct straight lines.

In the region represented by the blue line, the MSD slope exhibits a slow increase with temperature. This indicates that temperature changes within this range have a relatively minor effect on the mobility of PA6, as the polymer remains in a glassy state during this time. In contrast, in the region represented by the red line, the MSD slope displays a rapid increase with temperature. This suggests that temperature changes within this range have a significant effect on the mobility of PA6, indicating that the polymer undergoes a transition into a rubbery state. The glass transition occurs at a temperature of approximately 320 K. Polymers in the glassy state exhibit superior mechanical properties compared to those in the rubbery state.[48,52,53] Therefore, this can explain the observed shift in the failure mode. During low-temperature stretching, PA6 exists in a glassy state, where it exhibits reduced mobility and requires more energy to deform. Additionally, extracting polymer chains from the PA6 cluster becomes more challenging. Hence, the dominant failure mode is adhesive failure. Conversely, during high-temperature stretching, PA6 undergoes a glass transition, entering a rubbery state. This transition results in a substantial increase in the mobility of the polymer, making the extraction of polymer chains from the PA6 cluster significantly easier. Consequently, the dominant failure mode changes to cohesive failure.

4. DISCUSSION

On the basis of our simulation observations, we have some key findings. First, the interfacial properties of C/PA6 were found to improve with higher forming temperatures. This improvement can be attributed to the diffusion of PA6 atoms within the interface-forming region at elevated temperatures, leading to the formation of interfaces through nonbonded interactions with graphene atoms. Moreover, the interfacial bonding energy of C/PA6 exhibited a considerable increase after the cooling process, highlighting the influential role of cooling in the interfacial properties. Additionally, the C/PA6 interfaces that were prepared at higher forming temperatures displayed enhanced mechanical interfacial properties, and there was a noteworthy transition in the dominant failure mode from adhesive failure to cohesive failure with increasing forming temperature. Second, as the loading temperature increased, PA6 transitioned from a glassy state to a rubbery state, resulting in a substantial decline in its mechanical properties. Consequently, this transition led to a significant decrease in the mechanical properties of the C/PA6 interface near the glass transition temperature, accompanied by a shift in the dominant failure mode from adhesive failure to cohesive failure.

Our findings provide a fundamental understanding of the effect of temperature on the carbon fiber and PA6 interface from an atomistic point of view. Nanoscale properties are necessary for mesoscale and macroscale modeling. Unfortunately, advanced nanoscale experimental techniques, such as atomic force microscopy,[54−56] nanoindentation testing,[57−59] and nanoscale Fourier transform infrared spectroscopy,[60,61] are only able to measure interfacial properties at the nanoscale, not the dynamic evolution of interfaces. Thus, MD simulations are possibly the only effective tool at this point in time that can study the dynamic evolution of interfaces and the factors that affect this evolution.

We remark that complete CF3DP is a very complex process in reality, as it includes melting, impregnation, solidification, crystallization, and other multiphysics phenomena. It is quite challenging to model the whole process and predict the properties of the parts. With the size and time scale limitations of MD simulations,[62−64] we would like to give it a shot to investigate how the historical high-temperature equilibrium affects the interfacial properties qualitatively in this work. Additionally, we would like to illustrate the possibility of including the processing effect in MD simulations, which, if possible, would provide a new modeling strategy of the forming process from an atomistic point of view.

5. CONCLUSION

In this study, we utilized MD simulations to investigate the effect of temperature on the interfacial properties of C/PA6 fabricated using a continuous fiber 3D printing process. We found that the interfacial properties of C/PA6 were improved with higher forming temperatures, and this was due to the diffusion of PA6 atoms within the interface. Furthermore, it was observed that as the loading temperature increased, PA6

https://doi.org/10.1021/acsami.3c12372
ACS Appl. Mater. Interfaces XXXX, XXX, XXX−XXX

transitioned from a glassy state to a rubbery state, resulting in a substantial decline in its mechanical properties. Our study provides fundamental insights into the forming and failure processes of interfaces in CFRTPCs, offering a potential micromechanical model to bridge the gap between the microscopic and macroscopic perspectives of 3D-printed composites. These findings have practical implications for optimizing the fabrication process and understanding the performance of such composite materials in real-world applications.

AUTHOR INFORMATION

Corresponding Authors

Xin Yan − *School of Mechanical Engineering and Automation, Beihang University, Beijing 100191, China; Ningbo Institute of Technology, Beihang University, Ningbo, Zhejiang 315832, China;* orcid.org/0000-0002-6858-9152; Email: yan_xin@buaa.edu.cn

Wuxiang Zhang − *School of Mechanical Engineering and Automation, Beihang University, Beijing 100191, China; Ningbo Institute of Technology, Beihang University, Ningbo, Zhejiang 315832, China;* orcid.org/0000-0001-6141-3368; Email: zhangwuxiang@buaa.edu.cn

Yingdan Zhu − *Zhejiang Provincial Key Laboratory of Robotics and Intelligent Manufacturing Equipment Technology, Ningbo Institute of Material Technology and Engineering, Chinese Academy of Sciences, Ningbo, Zhejiang 315201, China;* orcid.org/0000-0001-8793-0777; Email: y.zhu@nimte.ac.cn

Authors

Shenru Wang − *School of Mechanical Engineering and Automation, Beihang University, Beijing 100191, China; Ningbo Institute of Technology, Beihang University, Ningbo, Zhejiang 315832, China;* orcid.org/0000-0002-9358-7618

Baoning Chang − *Ningbo Institute of Technology, Beihang University, Ningbo, Zhejiang 315832, China;* orcid.org/0000-0001-6565-4468

Siqin Liu − *School of Mechanical Engineering and Automation, Beihang University, Beijing 100191, China;* orcid.org/0000-0002-5175-8124

Lihua Shao − *School of Aeronautic Science and Engineering, Beihang University, Beijing 100191, China;* orcid.org/0000-0003-3694-0523

Xilun Ding − *School of Mechanical Engineering and Automation, Beihang University, Beijing 100191, China; Ningbo Institute of Technology, Beihang University, Ningbo, Zhejiang 315832, China;* orcid.org/0000-0002-9752-3937

Complete contact information is available at: https://pubs.acs.org/10.1021/acsami.3c12372

Notes

The authors declare no competing financial interest.

ACKNOWLEDGMENTS

This work was supported by the Zhejiang Provincial Natural Science Foundation of China (LD22E050011), the Ningbo Key Projects of Science and Technology Innovation 2025 Plan (2022Z070), the National Natural Science Foundation of China (NSFC, 12372106 and 12272020), the Opening Funding of State Key Laboratory of Structural Analysis for Industrial Equipment, Dalian University of Technology (GZ22101), and the Start-up Youth Fundation of Ningbo Institute of Technology, Beihang University (NBQN202104001). We extend our heartfelt gratitude to Professor Zhijian Wang of the School of Materials Science and Engineering at Beihang University for his invaluable assistance and support.

REFERENCES

(1) Kwon, D.-J.; Kim, N.-S.-R.; Jang, Y.-J.; Choi, H. H.; Kim, K.; Kim, G.-H.; Kong, J.; Nam, S. Y. Impacts of Thermoplastics Content on Mechanical Properties of Continuous Fiber-Reinforced Thermoplastic Composites. *Compos. Part B* **2021**, *216*, 108859.

(2) Zheng, H.; Zhang, W.; Li, B.; Zhu, J.; Wang, C.; Song, G.; Wu, G.; Yang, X.; Huang, Y.; Ma, L. Recent Advances of Interphases in Carbon Fiber-Reinforced Polymer Composites: A Review. *Compos. Part B* **2022**, *233*, 109639.

(3) Yan, Y.; Xu, J.; Zhu, H.; Xu, Y.; Wang, M.; Wang, B.; Yang, C. Molecular Dynamics Simulation of the Interface Properties of Continuous Carbon Fiber/Polyimide Composites. *Appl. Surf. Sci.* **2021**, *563*, 150370.

(4) Huang, W.; Xu, R.; Yang, J.; Huang, Q.; Hu, H. Data-Driven Multiscale Simulation of FRP Based on Material Twins. *Compos. Struct.* **2021**, *256*, 113013.

(5) Alshammari, B. A.; Alsuhybani, M. S.; Almushaikeh, A. M.; Alotaibi, B. M.; Alenad, A. M.; Alqahtani, N. B.; Alharbi, A. G. Comprehensive Review of the Properties and Modifications of Carbon Fiber-Reinforced Thermoplastic Composites. *Polymers* **2021**, *13*, 2474.

(6) Offringa, A. R. Thermoplastic Composites—Rapid Processing Applications. *Compos. Part A* **1996**, *27*, 329−336.

(7) Goh, G. D.; Toh, W.; Yap, Y.; Ng, T.; Yeong, W. Additively Manufactured Continuous Carbon Fiber-Reinforced Thermoplastic for Topology Optimized Unmanned Aerial Vehicle Structures. *Compos. Part B* **2021**, *216*, 108840.

(8) Markarian, J. Long Fibre Reinforced Thermoplastics Continue Growth in Automotive. *Plast. Addit. Compd.* **2007**, *9*, 20−24.

(9) Anandakumar, P.; Timmaraju, M. V.; Velmurugan, R. Development of Efficient Short/Continuous Fiber Thermoplastic Composite Automobile Suspension Upper Control Arm. *Mater. Today Proc.* **2021**, *39*, 1187−1191.

(10) Rubino, F.; Nisticò, A.; Tucci, F.; Carlone, P. Marine Application of Fiber Reinforced Composites: A Review. *J. Mar. Sci. Eng.* **2020**, *8*, 26.

(11) Love, L. J.; Kunc, V.; Rios, O.; Duty, C. E.; Elliott, A. M.; Post, B. K.; Smith, R. J.; Blue, C. A. The Importance of Carbon Fiber to Polymer Additive Manufacturing. *J. Mater. Res.* **2014**, *29*, 1893−1898.

(12) Goh, G. D.; Yap, Y. L.; Agarwala, S.; Yeong, W. Y. Recent Progress in Additive Manufacturing of Fiber Reinforced Polymer Composite. *Adv. Mater. Technol.* **2019**, *4*, 1800271.

(13) Tian, X.; Todoroki, A.; Liu, T.; Wu, L.; Hou, Z.; Ueda, M.; Hirano, Y.; Matsuzaki, R.; Mizukami, K.; Iizuka, K.; et al. 3D Printing of Continuous Fiber Reinforced Polymer Composites: Development, Application, and Prospective. *Chin. J. Mech. Eng. Addit. Manuf. Front.* **2022**, *1*, 100016.

(14) Kong, X.; Luo, J.; Luo, Q.; Li, Q.; Sun, G. Experimental Study on Interface Failure Behavior of 3D Printed Continuous Fiber Reinforced Composites. *Addit. Manuf.* **2022**, *59*, 103077.

(15) Tian, X.; Liu, T.; Yang, C.; Wang, Q.; Li, D. Interface and Performance of 3D Printed Continuous Carbon Fiber Reinforced PLA Composites. *Compos. Part A* **2016**, *88*, 198−205.

(16) Puck, A.; Schürmann, H. Failure Analysis of FRP Laminates by Means of Physically Based Phenomenological Models. *Compos. Sci. Technol.* **2002**, *62*, 1633−1662.

(17) Flore, D.; Stampfer, B.; Wegener, K. Experimental and Numerical Failure Analysis of Notched Quasi-Unidirectional Laminates at Room Temperature and Elevated Temperature. *Compos. Struct.* **2017**, *160*, 128−141.

(18) Zhang, Y.; Sun, L.; Li, L.; Wei, J. Effects of Strain Rate and High Temperature Environment on the Mechanical Performance of Carbon Fiber Reinforced Thermoplastic Composites Fabricated by Hot Press Molding. *Compos. Part A* **2020**, *134*, 105905.
(19) Mohammadizadeh, M.; Imeri, A.; Fidan, I.; Elkelany, M. 3D Printed Fiber Reinforced Polymer Composites-Structural Analysis. *Compos. Part B* **2019**, *175*, 107112.
(20) Eftekhari, M.; Fatemi, A. Tensile Behavior of Thermoplastic Composites Including Temperature, Moisture, and Hygrothermal Effects. *Polym. Test.* **2016**, *51*, 151−164.
(21) Sorrentino, L.; de Vasconcellos, D. S.; D'Auria, M.; Sarasini, F.; Tirillò, J. Effect of Temperature on Static and Low Velocity Impact Properties of Thermoplastic Composites. *Compos. Part B* **2017**, *113*, 100−110.
(22) Wang, Y.; Zhang, J.; Fang, G.; Zhang, J.; Zhou, Z.; Wang, S. Influence of Temperature on the Impact Behavior of Woven-Ply Carbon Fiber Reinforced Thermoplastic Composites. *Compos. Struct.* **2018**, *185*, 435−445.
(23) Dou, H.; Cheng, Y.; Ye, W.; Zhang, D.; Li, J.; Miao, Z.; Rudykh, S. Effect of Process Parameters on Tensile Mechanical Properties of 3D Printing Continuous Carbon Fiber-Reinforced PLA Composites. *Materials* **2020**, *13*, 3850.
(24) Young, D.; Wetmore, N.; Czabaj, M. Interlayer Fracture Toughness of Additively Manufactured Unreinforced and Carbon-Fiber-Reinforced Acrylonitrile Butadiene Styrene. *Addit. Manuf.* **2018**, *22*, 508−515.
(25) Wang, X. Q.; Jian, W.; Buyukozturk, O.; Leung, C. K.; Lau, D. Degradation of Epoxy/Glass Interface in Hygrothermal Environment: An Atomistic Investigation. *Compos. Part B* **2021**, *206*, 108534.
(26) Zhang, M.; Jiang, B.; Chen, C.; Drummer, D.; Zhai, Z. The Effect of Temperature and Strain Rate on the Interfacial Behavior of Glass Fiber Reinforced Polypropylene Composites: A Molecular Dynamics Study. *Polymers* **2019**, *11*, 1766.
(27) Tam, L.-h.; Zhou, A.; Yu, Z.; Qiu, Q.; Lau, D. Understanding the Effect of Temperature on the Interfacial Behavior of CFRP-Wood Composite via Molecular Dynamics Simulations. *Compos. Part B* **2017**, *109*, 227−237.
(28) Lin, F.; Xiang, Y.; Shen, H.-S. Temperature Dependent Mechanical Properties of Graphene Reinforced Polymer Nanocomposites−A Molecular Dynamics Simulation. *Compos. Part B* **2017**, *111*, 261−269.
(29) Dandekar, C. R.; Shin, Y. C. Effect of Porosity on the Interface Behavior of an Al2O3−Aluminum Composite: A Molecular Dynamics Study. *Compos. Sci. Technol.* **2011**, *71*, 350−356.
(30) Zhang, C.; Chen, M.; Coasne, B.; Keten, S.; Derome, D.; Carmeliet, J. Hygromechanics of Softwood Cellulosic Nanocomposite with Intermolecular Interactions at Fiber-Matrix Interface Investigated with Molecular Dynamics. *Compos. Part B* **2022**, *228*, 109449.
(31) Zhang, L.; Bai, Z.; Liu, L. Exceptional Thermal Conductance Across Hydrogen-Bonded Graphene/Polymer Interfaces. *Adv. Mater. Interfaces* **2016**, *3*, 1600211.
(32) He, Q.; Wang, H.; Fu, K.; Ye, L. 3D Printed Continuous CF/PA6 Composites: Effect of Microscopic Voids on Mechanical Performance. *Compos. Sci. Technol.* **2020**, *191*, 108077.
(33) Li, C.; Browning, A. R.; Christensen, S.; Strachan, A. Atomistic Simulations on Multilayer Graphene Reinforced Epoxy Composites. *Compos. Part A* **2012**, *43*, 1293−1300.
(34) Tam, L.-h.; Jiang, J.; Yu, Z.; Orr, J.; Wu, C. Molecular Dynamics Investigation on the Interfacial Shear Creep Between Carbon Fiber and Epoxy Matrix. *Appl. Surf. Sci.* **2021**, *537*, 148013.
(35) Li, M.; Gu, Y.; Liu, H.; Li, Y.; Wang, S.; Wu, Q.; Zhang, Z. Investigation the Interphase Formation Process of Carbon Fiber/Epoxy Composites Using a Multiscale Simulation Method. *Compos. Sci. Technol.* **2013**, *86*, 117−121.
(36) Du, J.; Yang, C.; Ma, X.; Li, Q. Insights into the Conformation Changes of SARS-Cov-2 Spike Receptor-Binding Domain on Graphene. *Appl. Surf. Sci.* **2022**, *578*, 151934.
(37) Ikeshima, D.; Nishimori, F.; Yonezu, A. Deformation Modeling of Polyamide 6 and the Effect of Water Content Using Molecular Dynamics Simulation. *J. Polym. Res.* **2019**, *26*, 151.
(38) Li, H.; Zhang, H.; Cheng, X. The Effect of Temperature, Defect and Strain Rate on the Mechanical Property of Multi-Layer Graphene: Coarse-Grained Molecular Dynamics Study. *Physica E* **2017**, *85*, 97−102.
(39) Yang, G.; Li, L.; Lee, W. B.; Ng, M. C. Structure of Graphene and Its Disorders: A Review. *Sci. Technol. Adv. Mater.* **2018**, *19*, 613−648.
(40) Plimpton, S. Fast Parallel Algorithms for Short-Range Molecular Dynamics. *J. Comput. Phys.* **1995**, *117*, 1−19.
(41) Stukowski, A. Visualization and Analysis of Atomistic Simulation Data with OVITO−the Open Visualization Tool. *Model. Simul. Mater. Sci. Eng.* **2010**, *18*, 015012.
(42) Stuart, S. J.; Tutein, A. B.; Harrison, J. A. A Reactive Potential for Hydrocarbons with Intermolecular Interactions. *J. Chem. Phys.* **2000**, *112*, 6472−6486.
(43) Sun, H.; Mumby, S. J.; Maple, J. R.; Hagler, A. T. An Ab Initio CFF93 All-Atom Force Field for Polycarbonates. *J. Am. Chem. Soc.* **1994**, *116*, 2978−2987.
(44) Koloor, S. S. R.; Rahimian-Koloor, S.; Karimzadeh, A.; Hamdi, M.; Petrů, M.; Tamin, M. Nano-Level Damage Characterization of Graphene/Polymer Cohesive Interface Under Tensile Separation. *Polymers* **2019**, *11*, 1435.
(45) Moon, J.; Yang, S.; Cho, M. Interfacial Strengthening Between Graphene and Polymer Through Stone-Thrower-Wales Defects: Ab Initio and Molecular Dynamics Simulations. *Carbon* **2017**, *118*, 66−77.
(46) Xu, Z.; Chen, L.; Huang, Y.; Li, J.; Wu, X.; Li, X.; Jiao, Y. Wettability of Carbon Fibers Modified by Acrylic Acid and Interface Properties of Carbon Fiber/Epoxy. *Eur. Polym. J.* **2008**, *44*, 494−503.
(47) Liu, Y.; Gall, K.; Dunn, M. L.; Greenberg, A. R.; Diani, J. Thermomechanics of Shape Memory Polymers: Uniaxial Experiments and Constitutive Modeling. *Int. J. Plast.* **2006**, *22*, 279−313.
(48) Xie, R.; Weisen, A. R.; Lee, Y.; Aplan, M. A.; Fenton, A. M.; Masucci, A. E.; Kempe, F.; Sommer, M.; Pester, C. W.; Colby, R. H.; et al. Glass Transition Temperature from the Chemical Structure of Conjugated Polymers. *Nat. Commun.* **2020**, *11*, 893.
(49) Mohammadi, M.; Davoodi, J.; et al. The Glass Transition Temperature of PMMA: A Molecular Dynamics Study and Comparison of Various Determination Methods. *Eur. Polym. J.* **2017**, *91*, 121−133.
(50) Zhang, W.; Deng, X.; Sui, G.; Yang, X. Improving Interfacial and Mechanical Properties of Carbon Nanotube-Sized Carbon Fiber/Epoxy Composites. *Carbon* **2019**, *145*, 629−639.
(51) Pesetskii, S.; Jurkowski, B.; Olkhov, Y. A.; Bogdanovich, S.; Koval, V. Influence of a Cooling Rate on a Structure of PA6. *Eur. Polym. J.* **2005**, *41*, 1380−1390.
(52) Rahaman, A. B.; Giri, D.; Sarkar, A.; Patra, S. K.; Banerjee, D. Effect of Thermodynamic Glass Transition on Charge Transport Properties in a Benzodithieno-Imidazole Π-Conjugated Polymer: Fullerene Blend. *Mater. Res. Express.* **2019**, *6*, 115114.
(53) Smith, K. E.; Parks, S. S.; Hyjek, M. A.; Downey, S. E.; Gall, K. The Effect of the Glass Transition Temperature on the Toughness of Photopolymerizable (Meth) Acrylate Networks Under Physiological Conditions. *Polymer* **2009**, *50*, 5112−5123.
(54) Xu, M.; Yi, J.; Feng, D.; Huang, Y.; Wang, D. Analysis of Adhesive Characteristics of Asphalt Based on Atomic Force Microscopy and Molecular Dynamics Simulation. *ACS Appl. Mater. Interfaces* **2016**, *8*, 12393−12403.
(55) Nguyen, H. K.; Shundo, A.; Liang, X.; Yamamoto, S.; Tanaka, K.; Nakajima, K. Unraveling Nanoscale Elastic and Adhesive Properties at the Nanoparticle/Epoxy Interface Using Bimodal Atomic Force Microscopy. *ACS Appl. Mater. Interfaces* **2022**, *14*, 42713−42722.
(56) Nguyen, H. K.; Shundo, A.; Ito, M.; Pittenger, B.; Yamamoto, S.; Tanaka, K.; Nakajima, K. Insights into Mechanical Dynamics of Nanoscale Interfaces in Epoxy Composites Using Nanorheology

https://doi.org/10.1021/acsami.3c12372
ACS Appl. Mater. Interfaces XXXX, XXX, XXX−XXX

Atomic Force Microscopy. *ACS Appl. Mater. Interfaces* **2023**, *15*, 38029−38038.
(57) Hodzic, A.; Stachurski, Z.; Kim, J. K. Nano-Indentation of Polymer−Glass Interfaces Part I. Experimental and Mechanical Analysis. *Polymer* **2000**, *41*, 6895−6905.
(58) Hodzic, A.; Kalyanasundaram, S.; Kim, J.; Lowe, A.; Stachurski, Z. Application of Nano-Indentation, Nano-Scratch and Single Fibre Tests in Investigation of Interphases in Composite Materials. *Micron* **2001**, *32*, 765−775.
(59) Jiao, W.; Zheng, T.; Liu, W.; Jiao, W.; Wang, R. Molecular Dynamics Simulations of the Effect of Sizing Agent on the Interface Property in Carbon Fiber Reinforced Vinyl Ester Resin Composite. *Appl. Surf. Sci.* **2019**, *479*, 1192−1199.
(60) Zhang, B.; Liu, S.; Yin, L.; Tian, M.; Ning, N.; Zhang, L.; Wang, W. Nanoscale Analysis of the Interface of Dip Layer/Rubber in Fiber/Rubber Composites. *Polymer* **2022**, *262*, 125472.
(61) Goikoetxea, M.; Amenabar, I.; Chimenti, S.; Paulis, M.; Leiza, J. R.; Hillenbrand, R. Cross-Sectional Chemical Nanoimaging of Composite Polymer Nanoparticles by Infrared Nanospectroscopy. *Macromolecules* **2021**, *54*, 995−1005.
(62) Darbaniyan, F.; Yan, X.; Sharma, P. An Atomistic Perspective on the Effect of Strain Rate and Lithium Fraction on the Mechanical Behavior of Silicon Electrodes. *J. Appl. Mech.* **2020**, *87* (3), 031011.
(63) Yan, X.; Sharma, P. Time-Scaling in Atomistics and the Rate-Dependent Mechanical Behavior of Nanostructures. *Nano Lett.* **2016**, *16*, 3487−3492.
(64) Yan, X.; Cao, P.; Tao, W.; Sharma, P.; Park, H. S. Atomistic Modeling at Experimental Strain Rates and Timescales. *J. Phys. D* **2016**, *49*, 493002.

https://doi.org/10.1021/acsami.3c12372
ACS Appl. Mater. Interfaces XXXX, XXX, XXX−XXX